

Full length article

Confined chemical and structural states at dislocations in Fe-9wt%Mn steels: A correlative TEM-atom probe study combined with multiscale modelling



A. Kwiatkowski da Silva^a, G. Leyson^a, M. Kuzmina^a, D. Ponge^{a,*}, M. Herbig^a,
S. Sandlöbes^{a,b}, B. Gault^a, J. Neugebauer^a, D. Raabe^a

^a Max-Planck Institut für Eisenforschung, Max-Planck Str. 1, 40237 Düsseldorf, Germany

^b Institute of Physical Metallurgy and Metal Physics, RWTH Aachen University, 52056 Aachen, Germany

ARTICLE INFO

Article history:

Received 19 September 2016

Received in revised form

4 November 2016

Accepted 6 November 2016

Keywords:

Medium manganese steel

Austenite reversion

Solute-dislocation interaction

Correlative transmission electron microscopy/atom probe tomography

Strain ageing

Linear complexion

Multiscale modelling

ABSTRACT

We investigated a high-purity cold-rolled martensitic Fe-9wt%Mn alloy. Tensile tests performed at room temperature after tempering for 6 h at 450 °C showed discontinuous yielding. Such static strain ageing phenomena in Fe are usually associated with the segregation of interstitial elements such as C or N to dislocations. Here we show by correlative transmission electron microscopy (TEM)/atom probe tomography (APT) experiments that in this case Mn segregation to edge dislocations associated with the formation of confined austenitic states causes similar effects. The local chemical composition at the dislocation cores was investigated for different tempering temperatures by APT relative to the adjacent bcc matrix. In all cases the Mn partitioning to the dislocation core regions matches to the one between ferrite and austenite in thermodynamic equilibrium at the corresponding tempering temperature. Although a stable structural and chemical confined austenitic state has formed at the dislocation cores these regions do not grow further even upon prolonged tempering. Simulation reveals that the high Mn enrichment along the edge dislocation lines (25 at.%Mn at 450 °C) cannot be described merely as a Cottrell atmosphere formed by segregation driven by size interaction. Thermodynamic calculations based on a multiscale model indicate that these austenite states at the dislocation cores are subcritical and defect-stabilized by the compression stress field of the edge dislocations. Phenomenologically, these states are the 1D equivalent to the so-called complexions which have been extensively reported to be present at 2D defects, hence have been named linear complexions.

© 2016 Acta Materialia Inc. Published by Elsevier Ltd. All rights reserved.

1. Introduction

Medium manganese steels are of high scientific and commercial interest as they combine high strength and ductility with low material costs [1]. A broad range of mechanical properties can be achieved for these alloys by adjusting the thermomechanical treatment. Identification of the optimum thermomechanical processing for tuning these alloys for specific properties requires precise knowledge about the underlying deformation mechanisms, both at ambient and elevated temperatures [2,3]. In this context both, the segregation of solutes and the reversion from martensite into austenite can significantly alter the deformation behavior.

Grain boundary segregation can either cause catastrophic grain boundary embrittlement [4], or substantial strengthening [5], sensitively depending on the applied heat treatment. Segregation of solutes to dislocations (Cottrell atmospheres) [6] can cause upper and lower yield points, strain localization (Lüders bands) and a serrated stress-strain curve, often referred to as jerky flow, Portevin-Le Chatelier, or dynamic strain aging effect [6,7]. Such a behavior was mainly reported for the interstitial Fe-C and Fe-N systems in binary [6], ferritic [8] and martensitic alloys [9] and also in austenitic Fe-Mn-C TWIP steels [10]. Most reports on the strain aging behavior of iron-based interstitial-containing alloys assume that the interstitial-dislocation interaction is the governing mechanism (e.g. in Fe-18%Ni steel), as interstitials have a comparably high mobility and strongly interact with dislocations [11]. However, investigations of the FCC Cu-Al [12] and Cu-Mn systems [12] showed that static and dynamic strain aging is a general

* Corresponding author.

E-mail address: d.ponge@mpie.de (D. Ponge).

phenomenon, which can be observed even when no interstitial atoms are involved. Cottrell atmospheres composed of C [13,14], B [15], W [16], As [17], Cu and Mo [18,19], Cr and V [20,21] were observed in steels. Simulations predict an attractive driving force for equilibrium segregation of Mn to edge dislocations in ferrite [22] but so far, corresponding experimental evidence was only presented for the non-equilibrium segregation of Mn to dislocations in irradiated Eurofer 97 steel [19,21].

Mn segregation plays a key role in the formation of reverted austenite which enables the design of high strength and ductile medium manganese steels. Numerous works were devoted to explore new strategies of thermomechanical processing in order to understand and optimize austenite reversion times, morphology, size effects and the stability of the reverted austenite when exposed to mechanical loads [23–25]. Grain boundaries and dislocations are well-known sites for the nucleation of new phases in systems such as Fe–Au and Fe–Cu [26], for carbide nucleation in steels [27] and for the nucleation of martensite [28]. Heterogeneous nucleation at defects requires less activation energy than homogenous nucleation due to the reduction of the required interface energy. However, segregation to defects locally alters the chemical composition and thereby the thermodynamic driving force for phase transformations and can therefore have an additional strong effect for phase nucleation at decorated defects. If the local chemical composition at a defect comes close to the one of a new phase in thermodynamic equilibrium at the given temperature a local phase transformation at the defect can occur which would not happen without segregation [29,30]. This concept has been successfully applied to the development of martensitic medium manganese steels with high strength and ductility [1–4,31,32].

Since at least half a century, it has been speculated [33–37] that grain boundaries and other interfaces can be analyzed using local equilibrium thermodynamics and may transform in a manner analogous to bulk phases, although equilibrium interfacial states do not satisfy the Gibbs definition of a phase because they are inhomogeneous and may have gradients of structure, composition, properties and other parameters. Therefore, the term “complexion” was introduced in the literature to denote an equilibrium interfacial state and to emphasize the fact that they would not exist without the adjoining bulk phase(s) [38–41]. The existence of confined states (or complexions) at interfaces has been investigated since at least two decades, especially at grain boundaries by high-resolution scanning transmission electron microscopy (HRSTEM) as an attempt to explain phenomena such as abnormal grain growth (especially in alumina), grain boundary embrittlement (noteworthy in the systems Al–Ga, Ni–Bi, SiC and Si₃N₄) and activated sintering [38–40,42,43], that could not be successfully described before by purely mechanistic explanations. It has been recognized also that similar chemically and thermally induced structural transitions, analogous to grain boundary complexions, may also occur in the structure of dislocations, triple lines and quadruple junctions, which may affect the nucleation and propagation of cracks and alter the dislocation dynamics [40]. In a prior study, the current authors conducted correlative transmission electron microscopy – atom probe tomography (TEM–APT) investigations on the Fe–9wt%Mn system showing that the strain field of dislocations can induce state transitions which phenomenologically resemble complexion transitions [44]. The local chemical composition at the dislocation cores was investigated for different tempering temperatures by APT. It was observed that for each temperature the composition matched the Mn equilibrium partitioning content expected for the corresponding austenite when in equilibrium with adjacent ferrite. Since these states do not further grow even after prolonged tempering treatments, the authors introduced the term “linear complexion” in analogy to “planar complexions” to describe these subcritical

defect-stabilized states [44]. Here we present further experimental details including atom probe crystallography, introduce a theoretical model and discuss the underlying mechanisms and their consequences for the resulting properties associated with this linear complexion phenomenon.

2. Materials and methods

The binary Fe–9wt%Mn alloy was cast into a rectangular billet of 4 kg in a vacuum induction furnace. The slabs were hot-rolled at 1100 °C from 60 to 6 mm thickness and then water quenched. Subsequently, highly segregated edges of the slab were cut off. The billets were reheated to 1100 °C for 1 h and water quenched to room temperature to minimize Mn banding. Table 1 summarizes the chemical composition after homogenization according to wet chemical analysis. In the equilibrium state at room temperature the alloy composition is in the two phase region (ferrite and austenite). After water quenching from the homogenizing temperature the alloy is fully martensitic. Further tempering of the alloy for 6, 18 and 336 h at 450 °C in the two phase field was conducted in an air circulated furnace followed by water quenching.

Static strain ageing tensile testing was performed after 50% cold-rolling and tempering for 6 h at 450 °C on flat samples with a thickness, width and gauge length of 1 mm, 5 mm and 25 mm, respectively, at an initial strain rate of 10^{-3} s^{-1} at room temperature. Three samples were analyzed in total. For the tensile tests, a Kammrath and Weiss stage was used, and the strain was measured by digital image correlation (DIC) using Aramis software (GOM GmbH). Samples processed by 50% cold-rolling and tempering for 6 h at 450 °C were investigated by correlative TEM/APT using the experimental setup described in Ref. [45].

The atom probe specimens were prepared using a FEI Helios NanoLab 600i dual-beam FIB/SEM instrument. The specimens were extracted from the surface of the bulk material by the FIB lift-out procedure outlined by Thompson et al. [46], deposited on a bisected, electropolished TEM grid, sharpened to tip radii of below 100 nm and subsequently imaged by STEM and analyzed by APT as described by Herbig et al. [45]. APT characterization was conducted on a Cameca LEAP 3000X HR instrument, at a base temperature of $50 \pm 4 \text{ K}$, operated in laser-pulsed mode (wavelength 532 nm; pulse repetition rate: 250 kHz) with 0.4 nJ pulse energy. Reconstruction was carried out using commercial software (Cameca IVAS®) following the protocol introduced by Geiser et al. [47]. TEM images of the atom probe samples were used as templates to fine-tune parameters ensuring the correctness of the spatial dimensions in the reconstructed 3D atom maps. Alternatively, structural features extracted from atom probe tomography data, e.g. atomic planes [48], were used to calibrate the tomographic reconstruction and perform additional crystallographic analysis of the dislocations [49]. TEM was conducted in a JEOL JEM-2200FS operated at 200 kV.

3. Experimental observations

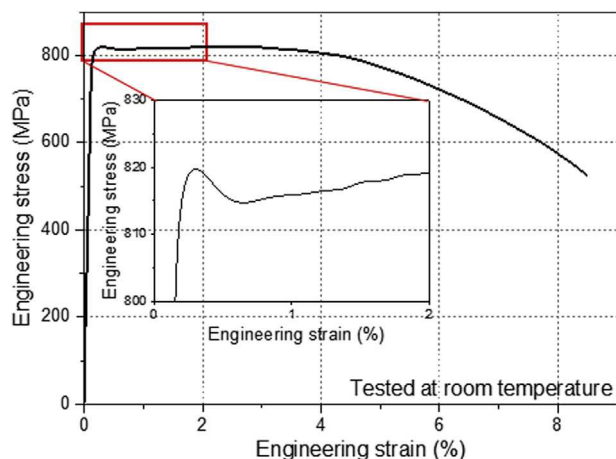
3.1. Mechanical behavior

Fig. 1 shows the result of a tensile test performed at room temperature with a strain rate of 10^{-3} s^{-1} on the 50% cold-rolled (to increase the dislocation density) and subsequently tempered (6 h at 450 °C) material. The slow strain rate was selected in order to avoid adiabatic heating. A drop in the stress level by 5 MPa after the onset of yielding is observed indicating a softening mechanisms which is attributed to the production of a sufficient density of mobile dislocations [6,50].

Table 1

Chemical composition of Fe-9wt%Mn in wt% according to wet-chemical analysis.

Mn	C	Ni	Co	Mo	Si	Al	S	P	O	N	Fe
8.46	0.0075	0.0175	0.0022	<0.002	0.0024	<0.002	0.0047	<0.002	0.0102	0.0040	balance

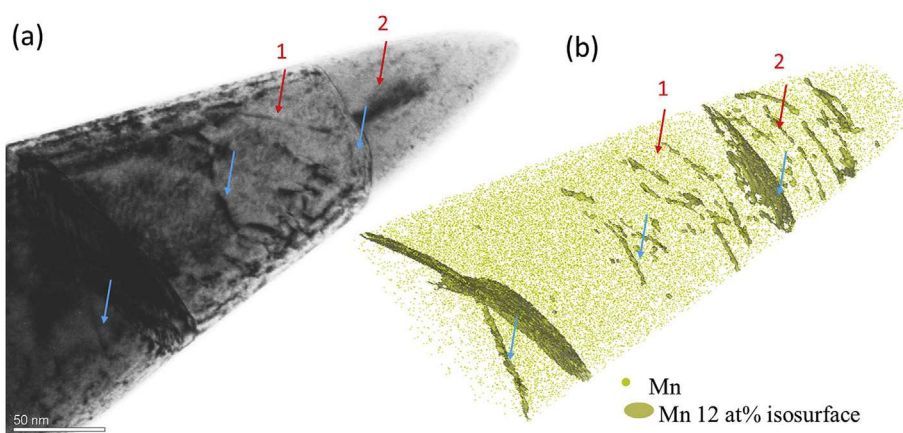
**Fig. 1.** Stress-strain curve of the material at room temperature after 50% cold-rolling and tempering at 450 °C for 6 h prior to testing. Static strain aging is observed.

3.2. Microstructure characterization

Performing TEM prior to APT on the same specimen allows to directly link structural information (TEM) with chemical information (APT) [44,45,51,52]. This enables in the current case the cross-correlation of lattice defects and associated local chemical inhomogeneities measured by APT. Fig. 2 depicts such a correlative STEM/atom probe analysis performed on the cold-rolled and tempered (6 h at 450 °C) material. Two low angle grain boundaries and a single dislocation, highlighted by blue arrows, are visible in both datasets. Not all dislocations visible in the STEM micrograph have solute enrichment that is sufficiently high to be detected by APT (red arrow 1). Also linear features enriched in Mn are visible in APT but not visible in the STEM image (red arrow 2). Fig. 3 presents two further examples of Mn enrichment to dislocation core regions after longer tempering times of 18 h and 336 h, respectively.

We performed both quantitative chemical analysis of the Mn enrichment at selected individual dislocations and of the average Mn enrichment to all dislocations observed. The chemical composition was investigated using two different approaches, namely, via one-dimensional concentration profiles taken along specific cylinder-shaped regions of interest, giving precise local composition information but poor statistics, and via proximity histogram analysis [53], which gives good statistics for the average Mn enrichment profile across the entire iso-concentration surface but it neglects local deviations. Concentration profiles were computed transverse and along individual dislocation lines as depicted in Fig. 4 and marked as (1), (3) and (2), (4), respectively. The analysis is related to the Fe-9wt%Mn alloy, 50% cold-rolled tempered at 450 °C for 6 h. The error bars represent statistical counting errors. A concentration of 25 ± 2 at.% Mn at the dislocation core is observed. When plotting 1D concentration profiles that intersect the dislocations at a 90° angle at certain points comparable peak concentrations of about 25–30 at.% Mn are observed. However, the 1-D concentration profiles plotted along straight dislocation line segments reveal that there are periodic changes in the Mn concentration with a spacing of ~5 nm along the dislocations (Fig. 4 (2), (4)). The morphology of Mn enrichment at the dislocations thus has a “pearl necklace-like” appearance (Fig. 4 (2), (4)). Both methods (1-D concentration profile and proximity histogram analysis) yield comparable results, namely, Mn enrichment of around 25 at.% at the core regions of the dislocations. This corresponds to an enrichment factor of 2.7 compared to the bulk concentration of Mn. The average thickness of the measured Mn-enriched zone is about 2 nm.

Fig. 5 shows an atom probe crystallographic analysis of the upper grain depicted in Fig. 2(b) (related to the Fe-9wt%Mn alloy, 50% cold-rolled tempered at 450 °C for 6 h). The {222} pole is directing upwards. All dislocations in the volume are positioned on either {112} or {123} planes, both of which are typical slip planes for the bcc system. Additionally, for each dislocation a <111> slip direction perpendicular to the dislocation line segment was found, identifying the associated dislocation character as edge type. The

**Fig. 2.** Correlative TEM/APT investigation of Fe-9wt%Mn alloy, 50% cold-rolled and subsequently tempered at 450 °C for 6 h for promoting Mn enrichment at lattice defects; (a) Bright-field STEM image; (b) Corresponding atom probe tomography measurement. Areas with Mn concentrations above 12 at% are highlighted by iso-concentration surfaces. The blue arrows mark grain boundaries and dislocations that are visible in both, the TEM micrograph and the 3D atom map. The analysis is conducted on an APT data set that was taken from Ref. [44]. (For interpretation of the references to colour in this figure legend, the reader is referred to the web version of this article.)

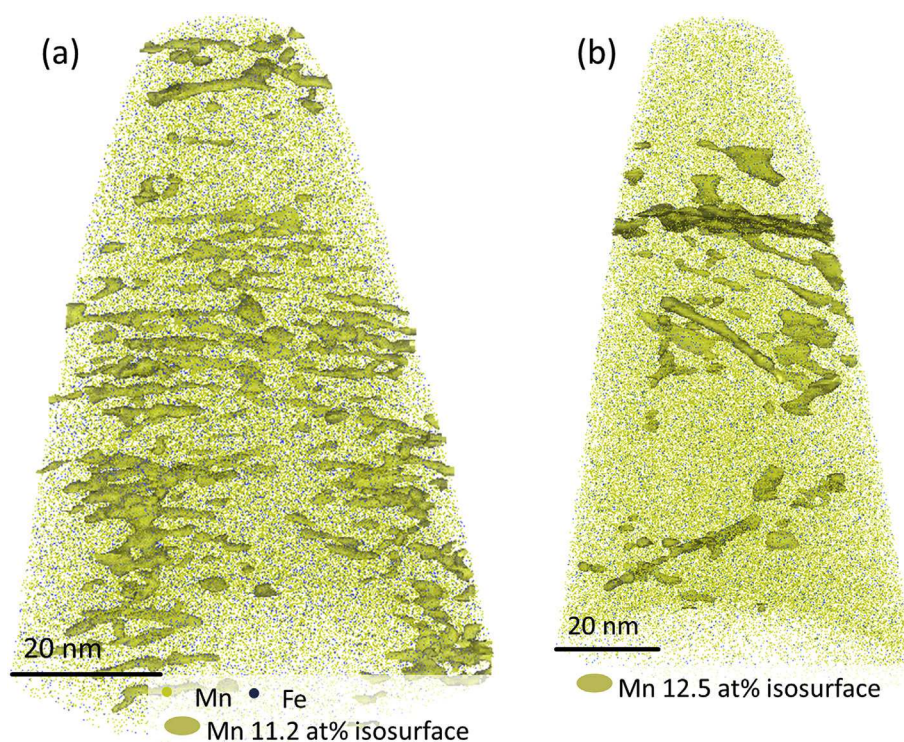


Fig. 3. Fe-9wt%Mn alloy, 50% cold-rolled and subsequently tempered at 450 °C for (a) 18 h and (b) 336 h; Mn enrichment to dislocation is clearly visible in both cases.

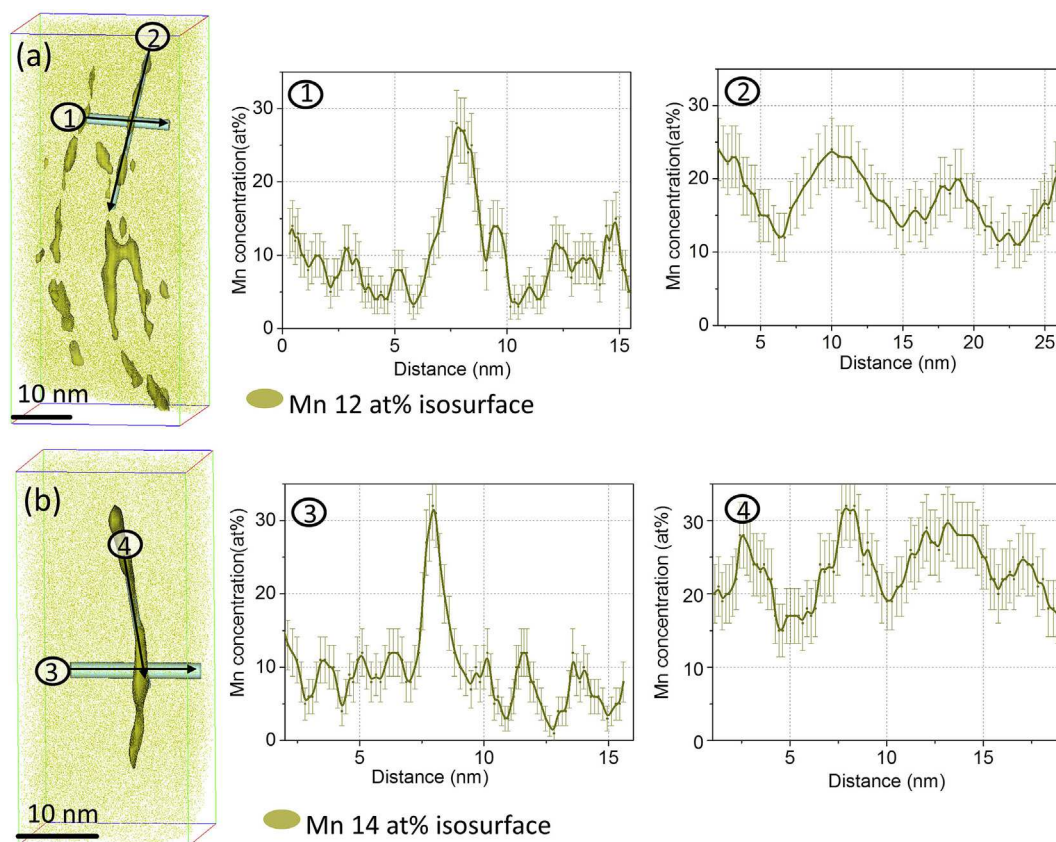


Fig. 4. 1D concentration analyses along cylindrical regions of interest of individual dislocations in Fe-9wt%Mn alloy, 50% cold-rolled tempered at 450 °C for 6 h (a) and (b) show examples from different samples. (1,3) mark concentration profiles transverse and (2,4) along the dislocations with cylinder diameters of 2 nm and 1 nm, respectively.

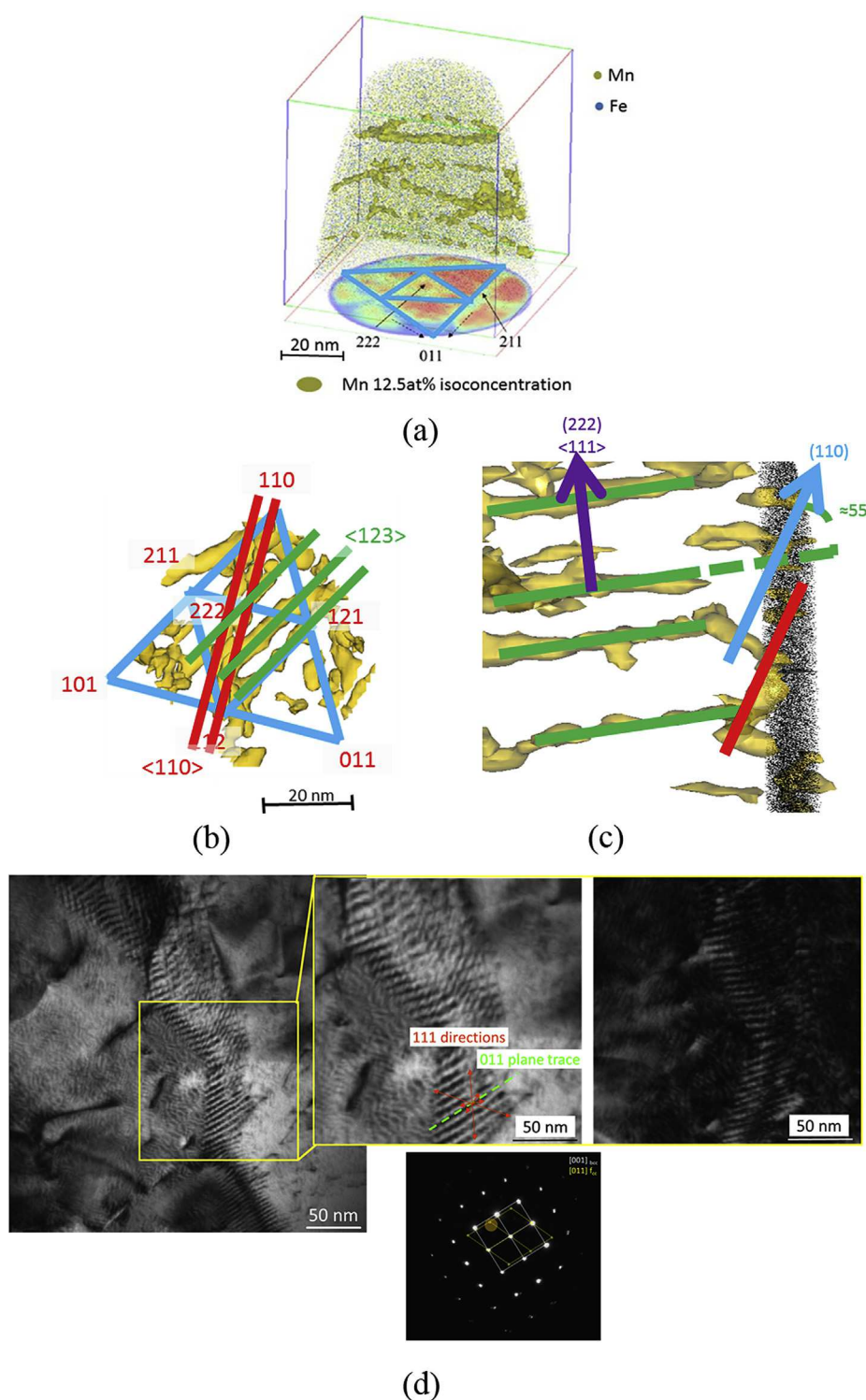


Fig. 5. Atom probe crystallographic analysis performed on the sub-region of the upper grain depicted in Fig. 2b (a–c) (relative to the Fe-9wt%Mn alloy, 50% cold-rolled tempered at 450 °C for 6 h), and associated transmission electron microscopy (TEM) analysis (d). (a) 3D atom map and corresponding projection of the volume's density along the tip axis. The density plot reveals the presence of a pole with a clear three-fold symmetry which is identified as a (222) pole. (b) Top view of the reconstructed volume shown in (a) with superposed stereographic projection. For clarity, no atoms are displayed. The {110} and {123} bcc slip planes that coincide with the dislocations visible in form of Mn enrichments are highlighted as straight red and green lines. (c) Angle to different sets of (011) planes observed in the tomographic reconstruction allows for unambiguous identification of the orientation of the dislocation and of the $\langle 111 \rangle$ slip direction which is perpendicular to the dislocation lines (edge dislocations). (d) TEM analysis on the same materials shows the presence of a fcc phase along the edge dislocation line segments. The dark field TEM micrograph is taken from the fcc area in the diffraction pattern as indicated by the yellow circle. Crystallographic analysis shows $\langle 111 \rangle$ slip direction at a 90° angle to the dislocation line segments, as indicated by the projections of the $\langle 111 \rangle$ directions in the bright field micrograph. (For interpretation of the references to colour in this figure legend, the reader is referred to the web version of this article.)

same crystallographic analysis was performed on further datasets with the same outcome. An analogous TEM analysis was performed on the same material (Fig. 5) following the procedure described in Ref. [44]. Fig. 5 (d) shows a small angle grain boundary composed of an array of dislocations where the dark field image is taken from the area of fcc spots in the {001} zone axis as indicated by the yellow circle in the diffraction pattern. The low contrast is due to the small volume fraction of fcc and the accordingly high exposure time needed to record the image. In the TEM image the {001} plane trace and the projections of $\langle 111 \rangle$ slip directions, as obtained by tilting experiments, are also shown. The transformed dislocation segments lie on {110} planes and with a $\langle 111 \rangle$ slip direction standing vertical to the line segments confirming that these dislocations segments have edge character. It might be surprising to observe such high density of edge dislocations in a bcc material. Edge dislocations in bcc Fe have much higher mobility at room temperature than screw dislocations and therefore in bcc microstructures deformed at room temperature mainly screw dislocations are observed [54,55]. We explain this observation by the high degree of preceding cold deformation in this Fe-9wt%Mn alloy and to the pinning effect exerted by the compositional decoration of the dislocation core regions. 50% cold-rolling was performed to increase the dislocation density in this material. The resulting dislocation interactions create highly entangled dislocation networks and small angle grain boundaries which immobilizes many of the edge dislocation segments. This cold-rolled material is hence assumed to contain an even higher density of screw dislocations than edge dislocations which, however, are not visible in the APT reconstructions as they are not decorated by Mn.

The concentration of 25 at% Mn measured at the edge dislocation cores at a tempering temperature of 450 °C corresponds to the thermodynamic equilibrium partitioning content of Mn in the austenite at this temperature. If austenite forms at dislocations the corresponding equilibrium Mn partitioning concentrations should also be observed for the cases of other tempering temperatures. Therefore, further atom probe experiments after tempering of the same material at 400 °C and 540 °C were conducted and an excellent agreement of the thermodynamically expected equilibrium partitioning Mn concentrations in austenite with the measured peak concentration at the dislocation core was found for all three temperatures studied. These observations indicate that the dislocation cores have indeed transformed into austenite. These results were previously reported elsewhere [44] and reproduced and adapted in Fig. 6. The same publication [44] also presents results of specimens subjected to extended isothermal tempering experiments (up to 336 h) revealing that the Mn-enriched zones are confined to the widths of the dislocation cores and do not grow beyond the dislocation core regions even upon long tempering treatments of up to several hundred hours.

4. Multiscale modelling

4.1. Transformation of dislocation cores

Strong elemental enrichment in conjunction with pronounced local elastic distortions may promote phase transformations [29]. Segregation-induced phase transformation has already been studied on grain boundaries in a medium Mn alloy [4] and can be well explained in terms of standard thermodynamic equilibrium calculations. The level of Mn enrichment on some dislocations in the tempered Fe-9wt%Mn alloy reaches the equilibrium concentration of Mn in austenite at the tempering temperatures of 400 °C, 450 °C and 540 °C, respectively, as outlined above [2].

We investigate this phenomenon by modelling the nucleation of austenite in a martensitic matrix containing an edge dislocation.

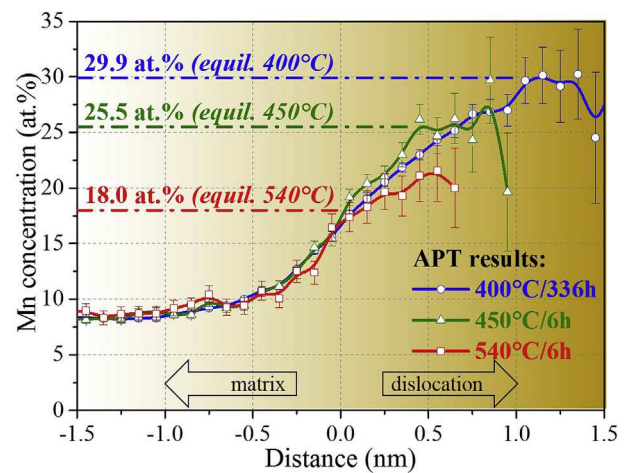


Fig. 6. Atom probe analysis of samples which were cold-rolled and tempered at three different temperatures: 400 °C, 450 °C and 540 °C. The plot contains Mn concentration profiles from the dislocation core outwards into the matrix, integratively measured over several dislocations via proximity histograms based on 14% iso-concentration surfaces. Mn concentrations of ~30, 25 at% Mn and 20 at%, respectively, at the dislocation core is observed for samples tempered at 400 °C, 450 °C and 540 °C, respectively. The thermodynamically predicted values at the respective temperature are marked by dashed lines. Adapted from Ref. [44].

The model is presented in Ref. [44], assumed an upper bound in the interaction between the complexion and the dislocation. In that analysis, it was assumed that the formation of the inclusion, i.e. of the transformed region, is able to remove all strain induced by the dislocation within the inclusion. This can be possible if mass transport is permitted and if only incoherent interfaces are considered. However, this is generally not true if the local phase forms coherent boundaries with the matrix. Additionally, the former analysis uses the more simple Volterra solution for the dislocation stress field, which is inaccurate for regions immediately adjacent to the dislocation core (where the linear complexion forms).

Therefore here we present a more advanced model which is illustrated schematically in Fig. 7. The local phase transition forms a pseudo-two-dimensional inclusion, characterized by a radius R and an eigenstrain ϵ_{ij}^* . The total free energy change of the system due to the formation of the inclusion is given by

$$\Delta F_{\text{tot}} = \Delta F_{\text{form}} + \Delta F_{\text{esh}} + \Delta F_{\text{int}} + \Delta F_{\gamma} \quad (1)$$

where ΔF_{form} is the change in energy due to the formation energy of the phase transformation, ΔF_{esh} is the self-energy of the Eshelby inclusion due to the eigenstrain ϵ_{ij}^* , ΔF_{int} is the interaction energy between the inclusion and the dislocation stress field $\sigma_{ij}^{\text{disl}}$ and ΔF_{γ} is the energy change due to the interface between the fcc inclusion

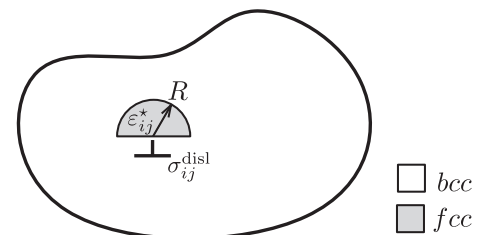


Fig. 7. Schematic representation of the current linear complexion phenomenon as an Eshelby problem. The linear complexion is modeled as a pseudo-two-dimensional inclusion in an infinite solid in the presence of an edge dislocation.

and the bcc matrix. The effect of the dislocation is encapsulated in the term ΔF_{int} , which is found to be always negative (favorable). To calculate ΔF_{tot} as accurately as possible, we used a multiscale approach, where we informed the continuum model outlined above with atomistic and first principles calculations.

4.2. Formation energy change, ΔF_{form}

We calculated the formation energy change using Density Functional Theory (DFT), as implemented in the Vienna Ab-initio Simulation Package (VASP) [56,57] in conjunction with Vanderbilt ultrasoft pseudopotentials [58], and the generalized gradient correction by Perdew and Wang [59,60]. The fcc and bcc structures were calculated assuming antiferromagnetic and ferromagnetic states, respectively. The results of the DFT calculations are summarized in Table 2.

Here, we assumed that the volume fraction of the inclusions is sufficiently small such that the nominal concentration of Mn in the surrounding bcc matrix remains unaffected by their formation. In this case, the system can be approximated by the grand canonical ensemble and the enthalpy of formation per atom Δh_{form} in the inclusion is given by

$$\Delta h_{\text{form}} = \Delta h_{(1-c)\text{Fe}-c\text{Mn}}^{\text{fcc}} - [(1-c)\mu_{\text{Fe}} + c\mu_{\text{Mn}}] \quad (2)$$

where, c is the concentration of Mn in the inclusion, $\Delta h_{(1-c)\text{Fe}-c\text{Mn}}^{\text{fcc}}$ is the enthalpy of austenite with Mn concentration c , and μ_{Fe} and μ_{Mn} are the chemical potentials of Fe and Mn, respectively. The last two terms were calculated from the bcc matrix with 9 at.%Mn. Using values from Table 2 gives $\Delta h_{\text{form}} = -11.3$ meV.

To calculate the free energy, the entropy per atom Δs should in principle be calculated. Although this quantity can also be calculated from first principles by considering all different contributions (e.g. configurational, vibrational, electronic, magnetic, etc.), such a calculation is computationally intensive and is beyond the scope of this paper. Instead, we assumed that the free energy change per atom Δf_{form} is on the order of Δh (i.e. 0 to -80 meV), which is consistent with the value calculated from Calphad using the Thermocalc TCFe7 Database, which predicts $\Delta f_{\text{form}} \sim -8.37$ meV, and explored the stability of the inclusion within that reasonable range.

4.3. Inclusion self-energy and interaction energy change

The inclusion self-energy ΔF_{esh} and the inclusion-dislocation interaction energy ΔF_{int} is given by the standard Eshelby inclusion problem in the presence of an external field,

$$\Delta F_{\text{esh}} = -\frac{1}{2} (S_{ijkl} C_{klmn} - C_{ijmn}) \epsilon_{mn}^* \epsilon_{ij}^* V_{\text{incl}}, \quad (3)$$

Table 2

Values for the formation energy change for fcc and bcc structures assuming anti-ferromagnetic and ferromagnetic states calculated using Density Functional Theory (DFT).

Formula	c_{Mn}	Energy/atom (eV)	Volume/atom (\AA^3)	$\Delta E/\text{Mn}$ (eV)
fcc Fe32	0.0%	−8.21	10.78	—
fcc Fe31Mn1	3.1%	−8.24	10.79	−0.93
fcc Fe28Mn4	12.5%	−8.33	10.80	−0.94
fcc Fe22Mn10	31.3%	−8.49	10.93	−0.89
fcc Fe21Mn11	34.4%	−8.52	10.95	−0.89
bcc Fe54	0.0%	−8.31	11.34	—
bcc Fe48Mn6	11.1%	−8.36	11.37	−0.43

$$\Delta F_{\text{int}} = -\bar{\sigma}_{ij}^{\text{disl}} \epsilon_{ij}^* V_{\text{incl}}, \quad (4)$$

where S_{ijkl} is the Eshelby tensor, C_{ijmn} is the stiffness tensor, $\bar{\sigma}_{ij}^{\text{disl}}$ is the average dislocation stress field inside the inclusion, and V_{incl} is the volume of the inclusion.

To determine the dislocation stress field $\sigma_{ij}^{\text{disl}}$ in the vicinity of the dislocation core, molecular static calculations were performed using the embedded atom potential (EAM) by Mendelev et al. [61], which accurately reproduces the dislocation structure calculated from first principles [62]. The full stress tensor is calculated using the standard virial expressions. The $\sigma_{11}^{\text{disl}}$ component of the stress is shown in Fig. 8.

For a cylindrical inclusion, the Eshelby tensor is given by Ref. [63]:

$$S_{1111} = S_{2222} = \frac{5-4\nu}{2(1-\nu)}, \quad (5)$$

$$S_{1122} = S_{2211} = \frac{3-4\nu}{2(1-\nu)}, \quad (6)$$

$$S_{1212} = \frac{3-8\nu}{8(1-\nu)}, \quad (7)$$

$$S_{1133} = S_{2233} = \frac{\nu}{2(1-\nu)}, \quad (8)$$

$$S_{2323} = S_{1313} = \frac{2-\nu}{4(1-\nu)}, \quad (9)$$

$$S_{3333} = S_{3311} = S_{3322} = 0. \quad (10)$$

The assumption of a cylindrical inclusion would lead to an underestimation of ΔF_{esh} , but the approximation is sufficient for the purposes of the analysis here. Errors in ΔF_{esh} due to this approximation can be considered as uncertainty in the formation energy ΔF_{form} , since both terms scale with the inclusion volume V_{incl} .

Since we assume that the inclusion forms a coherent interface with the matrix, the eigenstrain ϵ_{ij}^* requires careful consideration. Orientation relationships that produce large strains in the $\langle 111 \rangle$ -direction are energetically favored due to favorable elastic interaction with the large compressive stresses within the dislocation core (see Fig. 8). The orientation relationship (OR) that maximizes this interaction is $\{011\}_{\alpha}/\{011\}_{\gamma}$, which carries an eigenstrain of $\epsilon_{11}^* = -12.1\%$, $\epsilon_{22}^* = 1.5\%$ and $\epsilon_{33}^* = 7.7\%$. This OR would normally be unstable against more conventional ORs (e.g. Kurdjumov-Sachs, Nishiyama-Wassermann) in bulk, but is energetically more favorable in the compression region within the dislocation core.

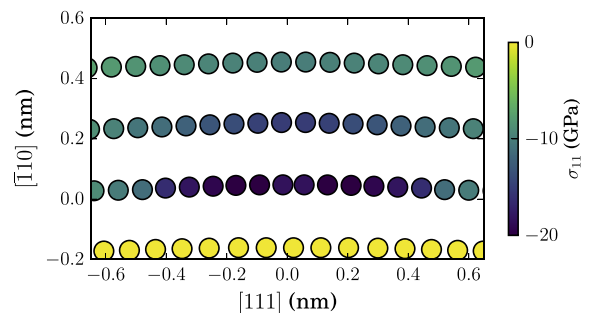


Fig. 8. The stress component $\sigma_{11}^{\text{disl}}$ as a function of position around the dislocation core region.

4.4. Interfacial energy

It is important to note that nucleation within the dislocation core is heterogeneous. In particular, formation of the inclusion in the compression region of the dislocation core replaces the stacking fault by a fcc-bcc interface. If we approximate the cross-section of the inclusion as a semicircle, schematically shown in Fig. 9, then the energy contribution due to the interface is

$$\Delta F_{\gamma} = \pi R L \gamma + 2 R L \Delta \gamma, \quad (11)$$

where L is the length of the inclusion, γ is the average interfacial energy between bcc and fcc, and $\Delta \gamma$ is the average difference between the bcc-fcc interfacial energy and the stacking fault energy. The stacking fault energy in bcc is relatively large, resulting in a very narrow dislocation core. For simplicity, we considered the case $\Delta \gamma / \gamma \ll 1$ and γ to be in the order of the literature value of 0.2 J/m^2 [64].

We conducted a parametric study of the energetics of the inclusion as a function of the inclusion radius R , the interfacial energy γ and the formation energy change per atom $\Delta f_{\text{form}} = \Delta F_{\text{form}} \Delta(V_{\text{Fe}}/V_{\text{incl}})$. From the analysis above, we looked at $0.1 \text{ J/m}^2 \leq \gamma \leq 0.6 \text{ J/m}^2$ and $-80 \text{ meV} \leq \Delta f_{\text{form}} \leq 0 \text{ meV}$, which are reasonable ranges for the system being considered. Fig. 10 shows a contour plot of the minimum radius R_{min} , showing three distinct regions. Representative plots for each region are shown in Fig. 11. When γ is large and Δf_{form} is large (Fig. 11(a)), the elastic penalty due to the coherency constraint dominates over the favorable formation energy and inclusion-dislocation interaction. In this case, nucleation is energetically unfavorable. On the other hand, if Δf_{form} is large (Fig. 11(b)), then nucleation is favorable, but the inclusion is unstable against coarsening (i.e. $R_{\text{min}} \rightarrow \infty$). However, if γ is small and Δf_{form} is not too small, it is possible to form a locally stable phase around the dislocation that is stable against coarsening (Fig. 11(c)).

Fig. 10 shows some interesting properties about the dislocation-stabilized local phase. First, there exists a maximum, above which the local transformation states cannot exist. This indicates that the local structural transformations are only possible for such states where they form coherent interfaces with the matrix, since incoherent boundaries have energies larger than 1 J m^{-2} [64]. Additionally, the local transformation state has a relatively narrow range of size ($R \sim 0.5\text{--}2 \text{ nm}$), which is roughly the size of the dislocation core. The model, therefore, predicts that the sizes of the local states are insensitive to temperature (which controls Δf_{form}). This prediction is consistent with the experimental observations (see Fig. 6).

5. Discussion

The discontinuous yielding observed in the tensile tests performed at room temperature on the tempered samples (Fig. 1) is

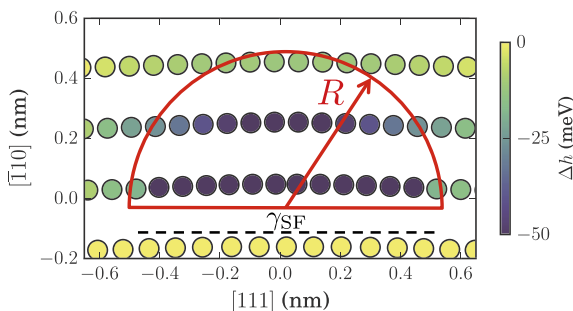


Fig. 9. Schematic representation of the inclusion cross-section.

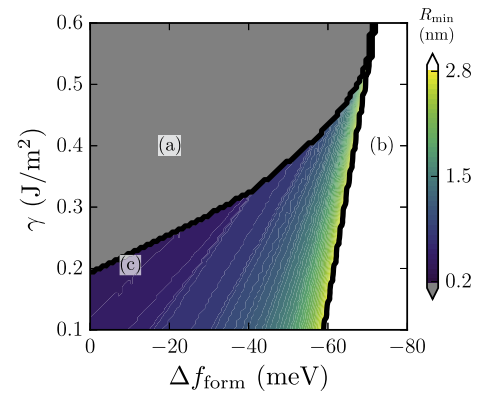


Fig. 10. Simulated equilibrium radius R_{min} of a local transformation state, represented in the current model as an inclusion, in the vicinity of an edge dislocation core region as a function of formation energy per atom Δf_{form} and interfacial energy γ .

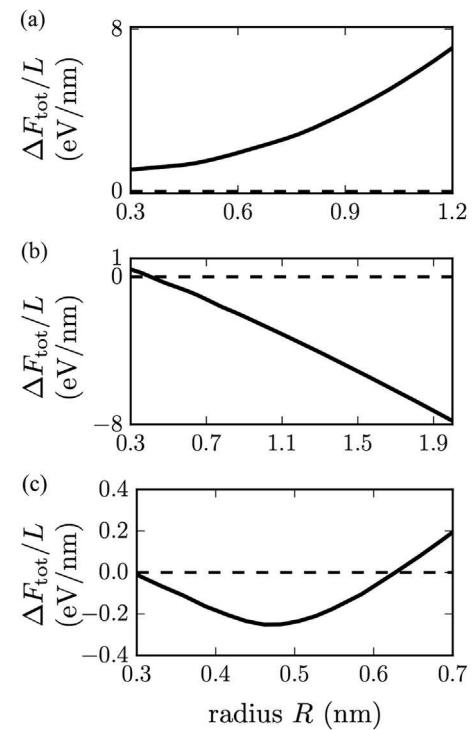


Fig. 11. Simulated change in free energy per unit length $\Delta F_{\text{tot}}/L$ as a function of the size R of a local transformation state at the dislocation core region, represented in the current model as an inclusion, for the following parameters: (a) $\Delta f_{\text{form}} = -20 \text{ meV}$ and $\gamma = 0.4 \text{ J/m}^2$, (b) $\Delta f_{\text{form}} = -75 \text{ meV}$ and $\gamma = 0.4 \text{ J/m}^2$, and (c) $\Delta f_{\text{form}} = -12 \text{ meV}$ and $\gamma = 0.2 \text{ J/m}^2$.

due to the static strain ageing effect. This phenomenon is commonly observed in materials where the dislocations are pinned by solutes and have to overcome a critical stress barrier to break free from the Cottrell atmospheres that were formed during aging or new mobile dislocations have to nucleate to accommodate deformation. However, in the present case, the edge dislocations are not blocked by substitutional Cottrell atmospheres but instead immobilized by confined transformation states, which we refer here to as linear complexions [44]. During cold-rolling prior to tempering, a high density of mobile dislocations was introduced into the microstructure. Upon subsequent tempering at 450°C the mobile edge dislocation segments were immobilized by solute enrichment or local phase transformation. Their spontaneous and

collective detachment and the formation of new mobile dislocations upon loading is therefore proposed to have caused the pronounced upper yield stress barrier and the discontinuous transition from the elastic into the elastic–plastic deformation regime. As this effect is observed here in a binary medium Mn alloy with very low C content of 0.0022 wt% and since only negligible amounts of C were found at the dislocations in APT, the pinning of dislocations is primarily attributed to Mn. Since only edge dislocation segments are immobilized in this case, screw segments are expected to be still mobile. This might result in an easy multiplication of mobile dislocations during straining and a rather small static aging effect on the yield point. In comparison, interstitial elements like C and N exhibit interactions with both edge and screw dislocations segments in the martensitic lattice due to its tetragonal distortion [65].

Our joint experimental and theoretical investigations indicate the formation of confined austenitic states at edge dislocation cores in an otherwise cubic martensitic matrix. The modelling introduced in this paper further indicates that these states are formed in the compression zone of edge dislocations, since the compression stress field can accommodate the contraction produced in the lattice by the formation of austenite. Additionally, edge dislocations are sinks of vacancies which allow fast diffusion of substitutional elements like Mn to the dislocation cores [66]. We assume that due to these two factors, only edge dislocations can act as effective sites for the formation of these confined austenitic states, as indicated by dislocation analysis using TEM and APT crystallography.

The current analysis shows that it is energetically favorable for fcc austenite to form in the immediate vicinity of the dislocation. However, the kinetic path that the system would take for this transformation to occur is beyond the scope of this work and remains to be determined. Nevertheless, some considerations are presented here, since our calculations indicate that Mn in bcc Fe has a slightly positive volume misfit and it is thus expected that Mn atoms would initially segregate to the tension side of the dislocation rather than to its compression side. Here, we tentatively propose the following hypotheses that might explain the kinetics of the process: First, even though Mn atoms are slightly larger than Fe, the misfit volume of Mn is relatively small ($<1 \text{ \AA}^3$) and one would expect a significant amount of Mn atoms in the tension side at the temperatures considered in experiments. Second, local fluctuations in the Mn concentration along the dislocation line might induce a section of the dislocation with statistically higher Mn concentration to locally transform from bcc to fcc with the help of the compression stress field, acting as embryo state of the linear complexions. Once such a transformation occurs, the local fcc phase would attract nearby Mn atoms, since Mn atoms prefer to partitioning from bcc into fcc, and the embryo would grow along the compression field of the dislocation line. Further, there might be a favorable interaction between Mn atoms and the stacking fault in the dislocation core [67,68]. If the interaction is favorable enough, then this can also act as a nucleus for the complexion. These hypotheses are to be explored by further calculations in the future.

As illustrated in Fig. 4 the Mn enrichment to dislocations has a “pearl-necklace-like” appearance, i.e. regions of higher and lower Mn enrichment alternate along the dislocation core. The periodicity of most regions is regular, although in some parts the regularity is clearly disturbed. These irregularities are attributed to a local change in the dislocation segment orientation. As shown earlier, only edge dislocation segments attract Mn atoms. The highly deformed material investigated here contains a high density of jogs and kinks located at the edge dislocations where a different Mn enrichment is expected. Similar observations of a concentration change due to the curvature of the grain boundaries were reported by Yao and Miller [69,70] and of dislocation loops by Hoummada [71] and Marquis [20]. The regions with periodic concentration

changes may arise due to a combination of various reasons: different lattice parameter between austenite and martensite; interface tension [72] and interface energy [73]. If there was a continuous transformation along the dislocation enormous strain would have to be accommodated along the dislocation line. Therefore, for energetic reasons the precipitation must alternate between segments with smaller and bigger lattice parameter along the dislocation line.

Such a confinement of a new structural state at a lattice defect resembles phenomenologically the concept of complexions: i.e. a defect-stabilized region in thermodynamic equilibrium with a structure and composition different from the surrounding matrix [38–40,42,43]. Up to the current case [44], complexions have only been observed on grain and phase boundaries [40,43]. Therefore, here we propose that solute enriched zones along dislocations can undergo complexion transitions, leading to the existence of confined chemical and structural states in local equilibrium with the dislocation stress field, as supported by the existence of a local minimum in the free energy curve for austenite formation. These confined states reduce the mobility of the abutting dislocations, as indicated by the discontinuous yielding observed in the tensile tests performed at room temperature on the tempered samples (Fig. 1). Therefore, the formation of linear complexions might be a new way for tailoring mechanical properties in advanced materials. Additionally, linear complexions possibly affect the kinetics of growth and morphology of second phases like austenite along low angle grain boundaries. Markedly, the formation of confined states at dislocations is a new microstructural finding that might offer new insights to explain different phenomena in materials science.

6. Conclusions

Static strain aging effects at 450 °C were observed in a binary Fe-9wt% Mn alloy and explained in terms of equilibrium enrichment of Mn atoms to edge dislocation segments. Using correlative TEM/APT analysis Mn-enriched cylindrical structures observed in 3D atom probe tomography maps could clearly be identified as decorated dislocation lines. TEM analysis and APT provided direct evidence for the formation of new structural states along the dislocation cores of dislocation edge segments. The Mn concentration in the dislocation core at the tempering temperatures 400 °C, 450 °C and 540 °C reaches levels of 30, 25, 20 at%, respectively, matching the respective Mn concentrations in austenite in thermodynamic partitioning equilibrium with a bcc matrix. Despite the fact that Mn enrichment at dislocations has triggered local transformation into austenite these structurally confined regions are unable to grow during extended isothermal tempering experiments, resembling phenomenologically the complexion concept. Thermodynamic and elastic considerations suggest that the complexion formation at dislocations are subcritical nuclei of austenite that are unable to grow for energetic reasons.

Acknowledgements

The authors gratefully acknowledge the ERC Advanced Grant “SMARTMET” for the funding of the work presented here. M. Herbig, J. Neugebauer, D. Ponge, D. Raabe and S. Sandlöbes are grateful to the German Research Foundation (Deutsche Forschungsgemeinschaft, DFG) for financial support through SFB761 “steel ab initio”. A. Kwiatkowski da Silva is grateful to the Brazilian National Research Council (Conselho Nacional de Pesquisas, CNPQ) for the PhD scholarship through the “Science without Borders” Project (203077/2014-8). U. Tezins & A. Sturm are acknowledged for their support to the users of the atom probe facility at MPIE.

References

- [1] D. Raabe, D. Ponge, O. Dmitrieva, B. Sander, Nanoprecipitate-hardened 1.5 GPa steels with unexpected high ductility, *Scr. Mater.* 60 (12) (2009) 1141–1144.
- [2] O. Dmitrieva, D. Ponge, G. Inden, J. Millán, P. Choi, J. Sietsma, D. Raabe, Chemical gradients across phase boundaries between martensite and austenite in steel studied by atom probe tomography and simulation, *Acta Mater.* 59 (1) (2011) 364–374.
- [3] D. Raabe, D. Ponge, O. Dmitrieva, B. Sander, Designing ultrahigh strength steels with good ductility by combining transformation induced plasticity and martensite aging, *Adv. Eng. Mater.* 11 (7) (2009) 547–555.
- [4] M. Kuzmina, D. Ponge, D. Raabe, Grain boundary segregation engineering and austenite reversion turn embrittlement into toughness: example of a 9 wt.% medium Mn steel, *Acta Mater.* 86 (2015) 182–192.
- [5] S.H. Song, R.G. Faulkner, P.E.J. Flewitt, Effect of boron on phosphorus-induced temper embrittlement, *J. Mater. Sci.* 34 (22) (1999) 5549–5556.
- [6] A.H. Cottrell, B.A. Bilby, Dislocation theory of yielding and strain ageing of iron, *Proc. Phys. Soc. Lond. Sect. A* 62 (349) (1949) 49–62.
- [7] A.H. Cottrell, A note on the portevin-le chatelier effect, *Philos. Mag.* 44 (355) (1953) 829–832.
- [8] A.K. De, S. Vandeputte, B.C. De Cooman, Kinetics of strain aging in bake hardening ultra low carbon steel - a comparison with low carbon steel, *J. Mater. Eng. Perform.* 10 (5) (2001) 567–575.
- [9] G.R. Speich, W.C. Leslie, Tempering of steel, *Metall. Trans.* 3 (5) (1972) 1043.
- [10] W.S. Owen, M. Grujicic, A Model of Solution Strengthening of Austenite by Carbon and Nitrogen, 1999.
- [11] S. Takaki, K.L. Ngo-Huynh, N. Nakada, T. Tsuchiyama, Strengthening mechanism in ultra low carbon martensitic steel, *Isij Int.* 52 (4) (2012) 710–716.
- [12] C. Schwink, A. Nortmann, The present experimental knowledge of dynamic strain ageing in binary f.c.c. solid solutions, *Mater. Sci. Eng. A Struct. Mater. Prop. Microstruct. Process.* 234 (1997) 1–7.
- [13] C.E. Hinchliffe, G.D.W. Smith, Strain aging of pearlitic steel wire during post-drawing heat treatments, *Mater. Sci. Technol.* 17 (2) (2001) 148–154.
- [14] J. Wilde, A. Cerezo, G.D.W. Smith, Three-dimensional atomic-scale mapping of a Cottrell atmosphere around a dislocation in iron, *Scr. Mater.* 43 (1) (2000) 39–48.
- [15] D. Blavette, E. Cadel, A. Fraczkiewicz, A. Menand, Three-dimensional atomic-scale imaging of impurity segregation to line defects, *Science* 286 (5448) (1999) 2317–2319.
- [16] M.K. Miller, Atom probe tomography characterization of solute segregation to dislocations, *Microsc. Res. Tech.* 69 (5) (2006) 359–365.
- [17] K. Thompson, P.L. Flaitz, P. Ronsheim, D.J. Larson, T.F. Kelly, Imaging of arsenic Cottrell atmospheres around silicon defects by three-dimensional atom probe tomography, *Science* 317 (5843) (2007) 1370–1374.
- [18] P.D. Styman, J.M. Hyde, K. Wilford, A. Morley, G.D.W. Smith, Precipitation in long term thermally aged high copper, high nickel model RPV steel welds, *Prog. Nucl. Energy* 57 (2012) 86–92.
- [19] G.D.W. Smith, D. Hudson, P.D. Styman, C.A. Williams, Studies of dislocations by field ion microscopy and atom probe tomography, *Philos. Mag.* 93 (28–30) (2013) 3726–3740.
- [20] E.A. Marquis, M. Bachhav, Y. Chen, Y. Dong, L.M. Gordon, A. McFarland, On the current role of atom probe tomography in materials characterization and materials science, *Curr. Opin. Solid State Mater. Sci.* 17 (5) (2013) 217–223.
- [21] C.A. Williams, J.M. Hyde, G.D.W. Smith, E.A. Marquis, Effects of heavy-ion irradiation on solute segregation to dislocations in oxide-dispersion-strengthened Eurofer 97 steel, *J. Nucl. Mater.* 412 (1) (2011) 100–105.
- [22] D. Udler, D.N. Seidman, Solute-atom interactions with low-angle twist boundaries, *Scr. Metall. Mater.* 26 (3) (1992) 449–454.
- [23] Y.K. Lee, J. Han, Current opinion in medium manganese steel, *Mater. Sci. Technol.* 31 (7) (2015) 843–856.
- [24] S. Lee, B.C. De Cooman, Influence of carbide precipitation and dissolution on the microstructure of ultra-fine-grained intercritically annealed medium manganese steel, *Metall. Mater. Trans. A Phys. Metall. Mater. Sci.* 47A (7) (2016) 3263–3270.
- [25] B. Sun, H. Aydin, F. Fazeli, S. Yue, Microstructure evolution of a medium manganese steel during thermomechanical processing, *Metall. Mater. Trans. A Phys. Metall. Mater. Sci.* 47A (4) (2016) 1782–1791.
- [26] E. Hornbogen, Role of strain energy during precipitation of copper and gold from alpha iron, *Acta Metall.* 10 (MAY) (1962) 525.
- [27] F.R. Beckitt, B.R. Clark, Shape and mechanism of formation of M23C6 carbide in austenite, *Acta Metall.* 15 (1) (1967) 113.
- [28] K.E. Easterling, A.R. Tholen, Nucleation of martensite in steel, *Acta Metall.* 24 (4) (1976) 333–341.
- [29] D. Raabe, S. Sandlöbes, J. Millán, D. Ponge, H. Assadi, M. Herbig, P.P. Choi, Segregation engineering enables nanoscale martensite to austenite phase transformation at grain boundaries: a pathway to ductile martensite, *Acta Mater.* 61 (16) (2013) 6132–6152.
- [30] D. Raabe, M. Herbig, S. Sandlöbes, Y. Li, D. Tytko, M. Kuzmina, D. Ponge, P.P. Choi, Grain boundary segregation engineering in metallic alloys: a pathway to the design of interfaces, *Curr. Opin. Solid State & Mater. Sci.* 18 (4) (2014) 253–261.
- [31] M.M. Wang, C.C. Tasan, D. Ponge, A. Kostka, D. Raabe, Smaller is less stable: size effects on twinning vs. transformation of reverted austenite in TRIP-maraging steels, *Acta Mater.* 79 (2014) 268–281.
- [32] M.M. Wang, C.C. Tasan, D. Ponge, A.C. Dippel, D. Raabe, Nanolaminate transformation-induced plasticity-twinning-induced plasticity steel with dynamic strain partitioning and enhanced damage resistance, *Acta Mater.* 85 (2015) 216–228.
- [33] E.W. Hart, 2-Dimensional phase transformation in grain boundaries, *Scr. Metall.* 2 (3) (1968) 179.
- [34] U. Erb, H. Gleiter, Effect of temperature on the energy and structure of grain-boundaries, *Scr. Metall.* 13 (1) (1979) 61–64.
- [35] H. Meiser, H. Gleiter, R.W. Mirwald, Effect of hydrostatic-pressure on the energy of grain-boundaries - structural transformations, *Scr. Metall.* 14 (1) (1980) 95–99.
- [36] J.W. Cahn, transitions and phase-equilibria among grain-boundary structures, *J. De Phys.* 43 (NC-6) (1982) 199–213.
- [37] C. Rottman, Theory of phase-transitions at internal interfaces, *J. De Phys.* 49 (C-5) (1988) 313–326.
- [38] M. Tang, W.C. Carter, R.M. Cannon, Diffuse interface model for structural transitions of grain boundaries, *Phys. Rev. B* 73 (2) (2006).
- [39] M. Tang, W.C. Carter, R.M. Cannon, Grain boundary transitions in binary alloys, *Phys. Rev. Lett.* 97 (7) (2006).
- [40] P.R. Cantwell, M. Tang, S.J. Dillon, J. Luo, G.S. Rohrer, M.P. Harmer, Grain boundary complexions, *Acta Mater.* 62 (2014) 1–48.
- [41] S.J. Dillon, K. Tai, S. Chen, The importance of grain boundary complexions in affecting physical properties of polycrystals, *Curr. Opin. Solid State Mater. Sci.*
- [42] S.J. Dillon, M. Tang, W.C. Carter, M.P. Harmer, Complexion: a new concept for kinetic engineering in materials science, *Acta Mater.* 55 (18) (2007) 6208–6218.
- [43] M.P. Harmer, The phase behavior of interfaces, *Science* 332 (6026) (2011) 182–183.
- [44] M. Kuzmina, M. Herbig, D. Ponge, S. Sandlöbes, D. Raabe, Linear complexions: confined chemical and structural states at dislocations, *Science* 349 (6252) (2015) 1080–1083.
- [45] M. Herbig, D. Raabe, Y.J. Li, P. Choi, S. Zaeferrer, S. Goto, Atomic-scale quantification of grain boundary segregation in nanocrystalline material, *Phys. Rev. Lett.* 112 (12) (2014).
- [46] K. Thompson, D. Lawrence, D.J. Larson, J.D. Olson, T.F. Kelly, B. Gorman, In situ site-specific specimen preparation for atom probe tomography, *Ultra-microscopy* 107 (2–3) (2007) 131–139.
- [47] B.P. Geiser, D.J. Larson, E. Oltman, S. Gerstl, D. Reinhard, T.F. Kelly, T.J. Prosa, Wide-field-of-view atom probe reconstruction, *Microsc. Microanal.* 15 (2009) 292–293.
- [48] B. Gault, F. de Geuser, L.T. Stephenson, M.P. Moody, B.C. Muddle, S.P. Ringer, Estimation of the reconstruction parameters for atom probe tomography, *Microsc. Microanal.* 14 (4) (2008) 296–305.
- [49] B. Gault, M.P. Moody, J.M. Cairney, S.P. Ringer, Atom probe crystallography, *Mater. Today* 15 (9) (2012) 378–386.
- [50] L.P. Kubin, Y. Estrin, C. Perrier, On static strain aging, *Acta Metall. Mater.* 40 (5) (1992) 1037–1044.
- [51] B.P. Gorman, A. Puthucode, D.R. Diercks, M.J. Kaufman, Cross-correlative TEM and atom probe analysis of partial crystallisation in NiNbSn metallic glasses, *Mater. Sci. Technol.* 24 (6) (2008) 682–688.
- [52] S.D. Walck, J.J. Hren, FIM/IAP/TEM studies of hydrogen in metals, *J. De Phys.* 45 (NC9) (1984) 355–360.
- [53] O.C. Hellman, J.A. Vandenbroucke, J. Rusing, D. Isheim, D.N. Seidman, Analysis of three-dimensional atom-probe data by the proximity histogram, *Microsc. Microanal.* 6 (5) (2000) 437–444.
- [54] S. Morito, X. Huang, T. Furuhara, T. Maki, N. Hansen, The morphology and crystallography of lath martensite in alloy steels, *Acta Mater.* 54 (19) (2006) 5323–5331.
- [55] B.P.J. Sandvik, C.M. Wayman, Characteristics of lath martensite .1. Crystallographic and substructural features, *Metall. Trans. A Phys. Metall. Mater. Sci.* 14 (5) (1983) 809–822.
- [56] G. Kresse, J. Furthmüller, Efficient iterative schemes for ab initio total-energy calculations using a plane-wave basis set, *Phys. Rev. B* 54 (16) (1996) 11169–11186.
- [57] G. Kresse, J. Hafner, AB-initio molecular-dynamics for open-shell transition-metals, *Phys. Rev. B* 48 (17) (1993) 13115–13118.
- [58] D. Vanderbilt, Soft self-consistent pseudopotentials in a generalized eigenvalue formalism, *Phys. Rev. B* 41 (11) (1990) 7892–7895.
- [59] J.P. Perdew, Y. Wang, Pair-distribution function and its coupling-constant average for the spin-polarized electron-gas, *Phys. Rev. B* 46 (20) (1992) 12947–12954.
- [60] J.P. Perdew, Y. Wang, Accurate and simple analytic representation of the electron-gas correlation-energy, *Phys. Rev. B* 45 (23) (1992) 13244–13249.
- [61] M.I. Mendelev, S. Han, D.J. Srolovitz, G.J. Ackland, D.Y. Sun, M. Asta, Development of new interatomic potentials appropriate for crystalline and liquid iron, *Philos. Mag.* 83 (35) (2003) 3977–3994.
- [62] A. Ramasubramanian, M. Itakura, E.A. Carter, Interatomic potentials for hydrogen in alpha-iron based on density functional theory, *Phys. Rev. B* 79 (17) (2009).
- [63] A. Bowen, *Applied Mechanics of Solids*, CRC Press, USA, 2009.
- [64] N. Nakada, T. Tsuchiyama, S. Takaki, N. Miyano, Temperature dependence of austenite nucleation behavior from lath martensite, *Isij Int.* 51 (2) (2011) 299–304.
- [65] G.A. Nematollahi, B. Grabowski, D. Raabe, J. Neugebauer, Multiscale description of carbon-supersaturated ferrite in severely drawn pearlitic wires, *Acta*

- Mater. 111 (2016) 321–334.
- [66] R. Bullough, R.C. Newman, Kinetics of migration of point defects to dislocations, Rep. Prog. Phys. 33 (2) (1970) 101.
- [67] T. Hickel, S. Sandlobes, R.K.W. Marceau, A. Dick, I. Bleskov, J. Neugebauer, D. Raabe, Impact of nanodiffusion on the stacking fault energy in high-strength steels, Acta Mater. 75 (2014) 147–155.
- [68] D. Raabe, F. Roters, J. Neugebauer, I. Gutierrez-Urrutia, T. Hickel, W. Bleck, J.M. Schneider, J.E. Wittig, J. Mayer, Ab initio-guided design of twinning-induced plasticity steels, Mrs Bull. 41 (4) (2016) 320–325.
- [69] M.K. Miller, L. Yao, Limits of detectability for clusters and solute segregation to grain boundaries, Curr. Opin. Solid State & Mater. Sci. 17 (5) (2013) 203–210.
- [70] L. Yao, S.P. Ringer, J.M. Cairney, M.K. Miller, The anatomy of grain boundaries: their structure and atomic-level solute distribution, Scr. Mater. 69 (8) (2013) 622–625.
- [71] K. Hoummada, D. Manginck, B. Gault, M. Cabie, Nickel segregation on dislocation loops in implanted silicon, Scr. Mater. 64 (5) (2011) 378–381.
- [72] Q. Liao, A.V. Dobrynin, M. Rubinstein, Counterion-correlation-induced attraction and necklace formation in polyelectrolyte solutions: theory and simulations, Macromolecules 39 (5) (2006) 1920–1938.
- [73] J. Zhu, X.F. Qian, Necklace-like nanostructures of cadmium hydroxide: controlled synthesis with bubble-template and its separation property on dye, Solid State Sci. 10 (11) (2008) 1577–1583.